Science Advances
AAAS

Supplementary Materials for

Geological, multispectral, and meteorological imaging results from the Mars 2020 Perseverance rover in Jezero crater

James F. Bell III *et al.*

Corresponding author: James F. Bell III, jim.bell@asu.edu

Sci. Adv. **8**, eabo4856 (2022)
DOI: 10.1126/sciadv.abo4856

The PDF file includes:

Figs. S1 to S11
Interactive 3D Models
Legends for movies S1 to S10

Other Supplementary Material for this manuscript includes the following:

Movies S1 to S10

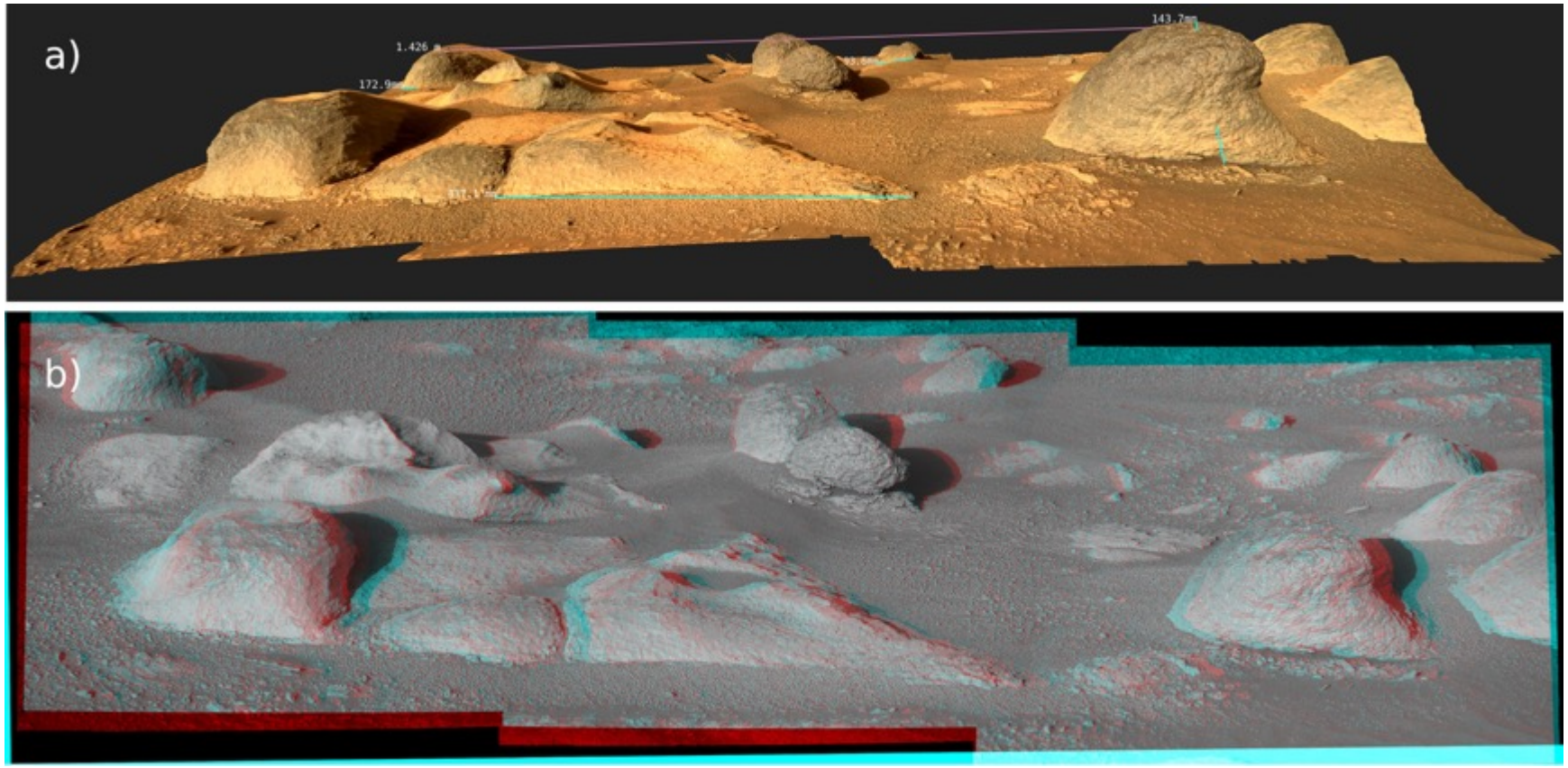

Figure S1. (a) Example Mastcam-Z 3D image and (b) stereo anaglyph (for red/blue glasses) of the darker toned rocks that stick out from the flat and low lying, polygonal fractured, and light-toned paver rocks of the Naat'áanii member of the Máaz formation, near the OEB landing site. Sol 88, zcam08047. The scene also shows the characteristics and distribution of regolith in this area of the rover traverse. Credits: NASA/JPL/Caltech/MSSS/ASU/JR/VRVis/ÖAW/Gerhard Paar.

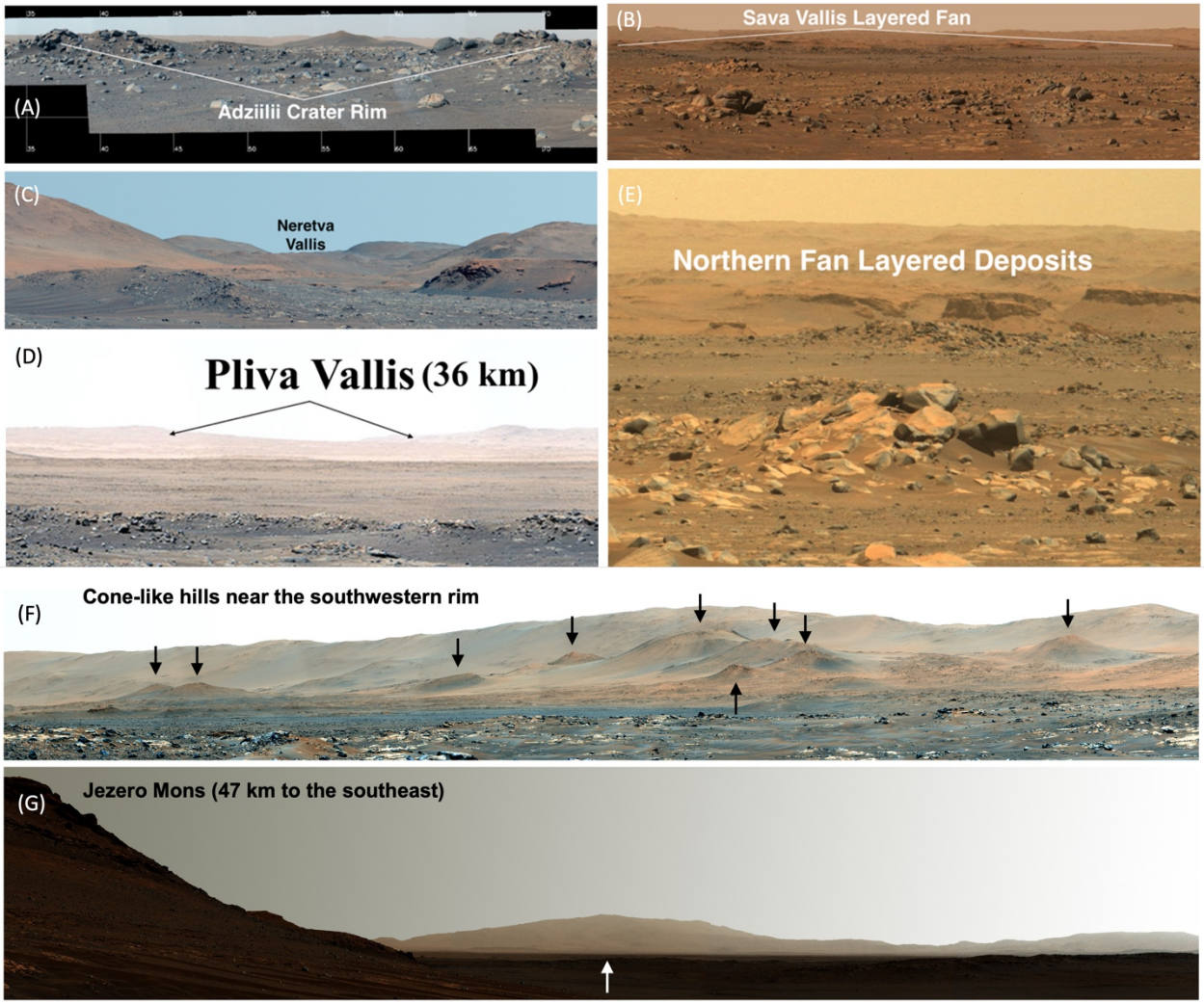

Figure S2. Examples of distant features imaged from the rover's landing site and along the traverse path (see also Figure 1). (A) Adziilii crater, Sol 112, zcam08088. Distance between the rim points noted is ~72 m; (B) Sava Vallis, Sol 53, zcam08100; (C) Neretva Vallis, Sol 275, zcam08134; (D) Pliva Vallis, Sol 132, zcam08134; (E) Zoomed view of the "northern fan" deposits at the mouth of Sava Vallis, Sol 63, zcam08108. The near-field boulders in the center of the image are each ~1 m across. (F) Enhanced color mosaic of examples of cone-like hills (arrows) approximately 10 km to the southwest of the OEB landing site, just within the rim (distant horizon) of Jezero crater. The hills range in height from 50 m to 300 m and in width from 330 m to 1.3 km. Sol 114, zcam08092. (G) Enhanced color mosaic of Jezero Mons (arrow), a large conical mountain outside of Jezero crater 47-km to the east-southeast of the landing site and rising ~2-km above the crater rim. The view is harshly contrast-enhanced to bring out subtle distant details. Sol 484, zcam08513.

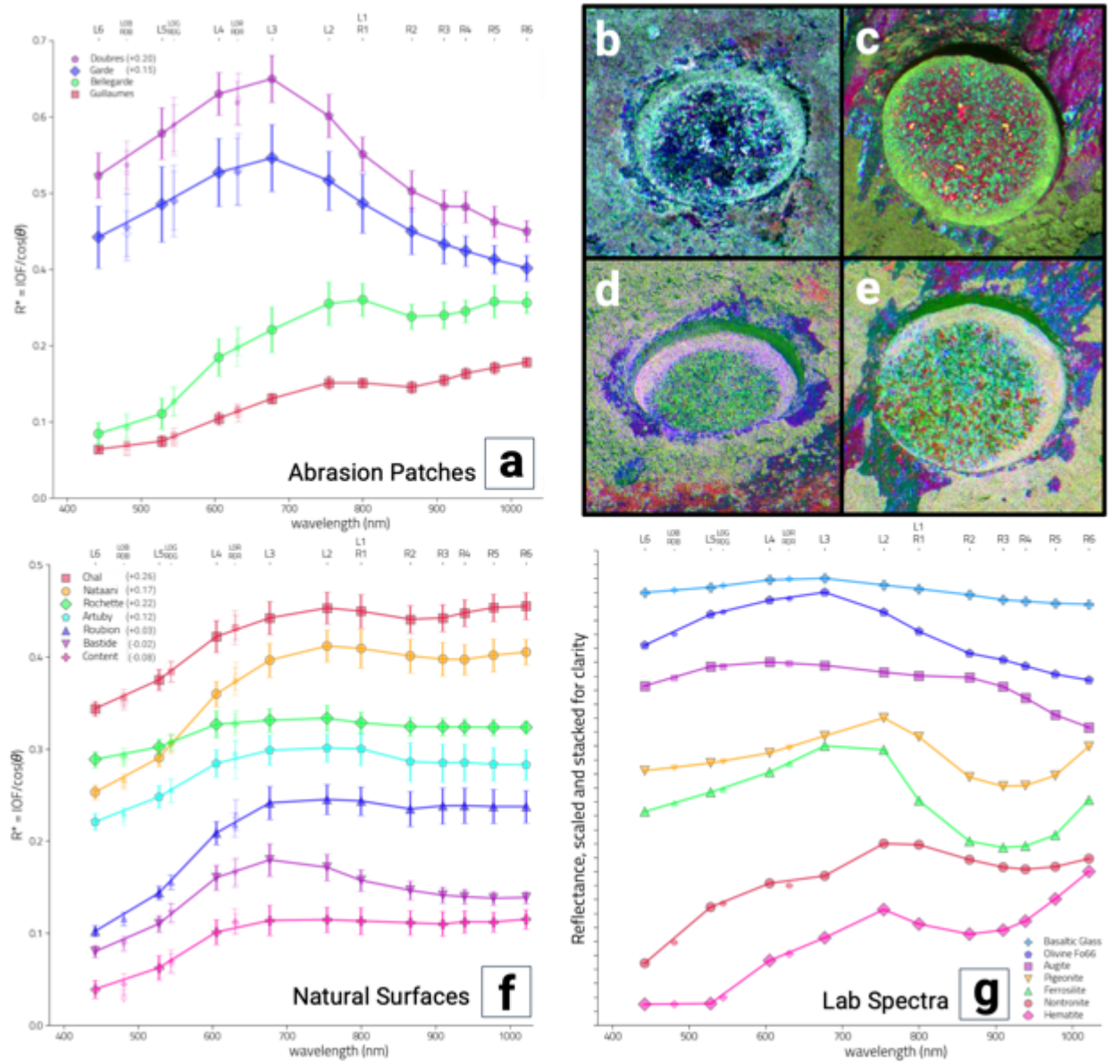

Figure S3. (a) Representative Mastcam-Z spectra from four abrasion patches, shifted vertically where indicated in legend, and shown as decorrelation stretch images (using filter L2,5,6): (b) Guillaumes (Sol 162, zcam03197, Roubion member); (c) Bellegarde (Sol 187, zcam3213, Rochette member); (d) Garde (Sol 207, zcam03229, Bastide member); (e) Dourbes (Sol 255, zcam03253, Bastide member). (f) For comparison, representative Mastcam-Z spectra from natural rock surfaces in each stratigraphic member, shifted vertically as indicated in legend, enhanced R0 Bayer filter context source images shown in Figure 8. (g) Laboratory spectra of relevant Fe-bearing minerals weighted by Mastcam-Z bandpasses, normalized and shifted for clarity: basaltic glass (*67*), olivine, ferrosilite, nontronite, hematite (*68*), pigeonite (*69*). For scale, each of the abrasion patches is 5 cm in diameter. Error bars represent spatial variance within each region sampled. See Table 1 for formation and member names associated with these sample sites.

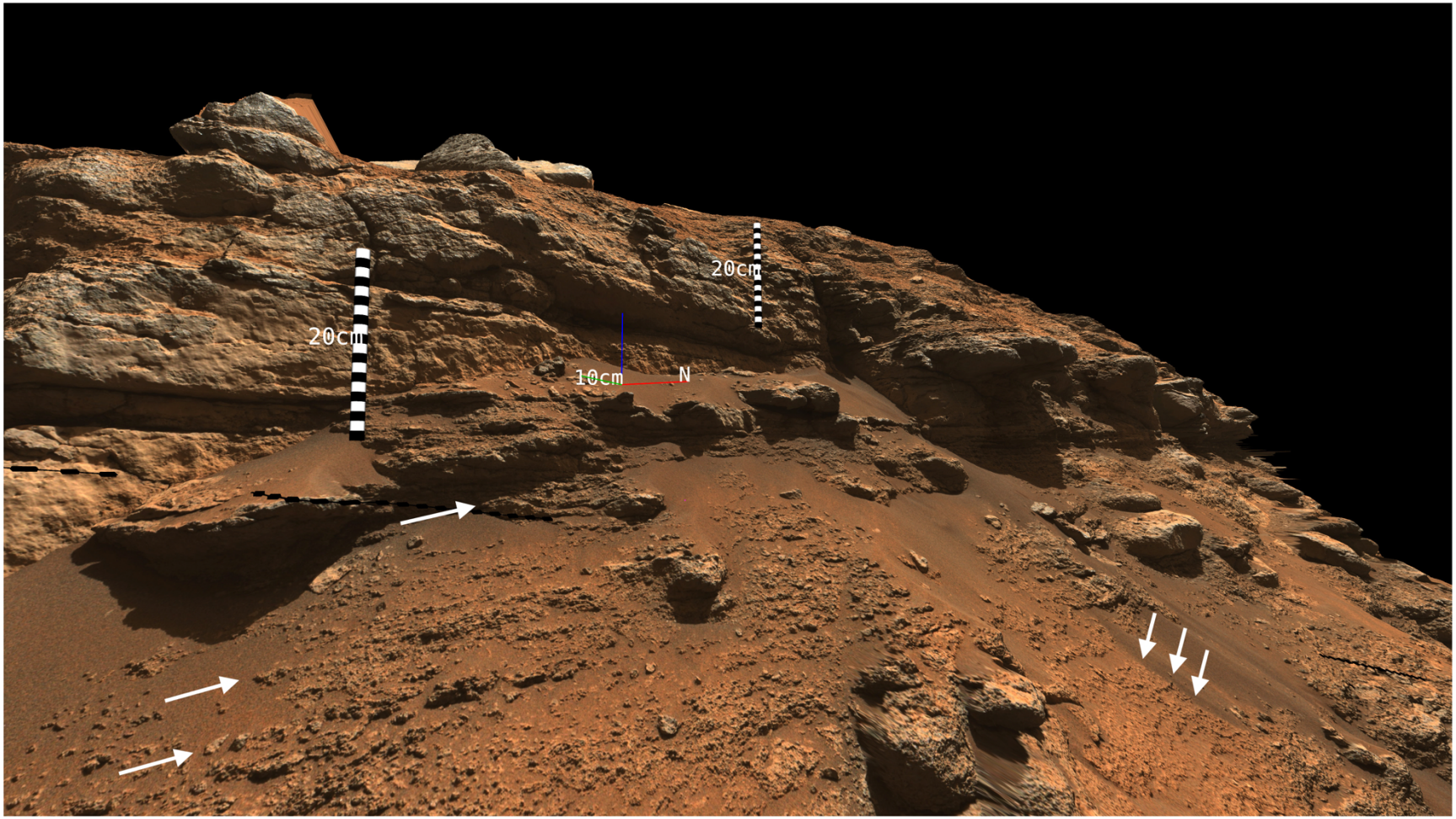

Figure S4. Example 3D reconstruction of an outcrop imaged by Mastcam-Z on Sol 177 (zcam08189) at the Artuby ridge, which is part of the Máaz formation. Massive decimeter scaled layers and centimeter to subcentimeter scaled layers are visible in the outcrop. The thin, planar layers with knobby textures (arrows) are reminiscent of sedimentary structures. Layers with a similar appearance are common throughout the Artuby ridge and also in some parts of the Mure outcrop. The massive and thicker layers dip with a mean (N=6) of 11.9°±1.2° towards south-southwest (azimuth of 209°±7°). See Materials and Methods. Credits: NASA/JPL/Caltech/MSSS/ASU/JR/VRVis/ÖAW/Andreas Bechtold.

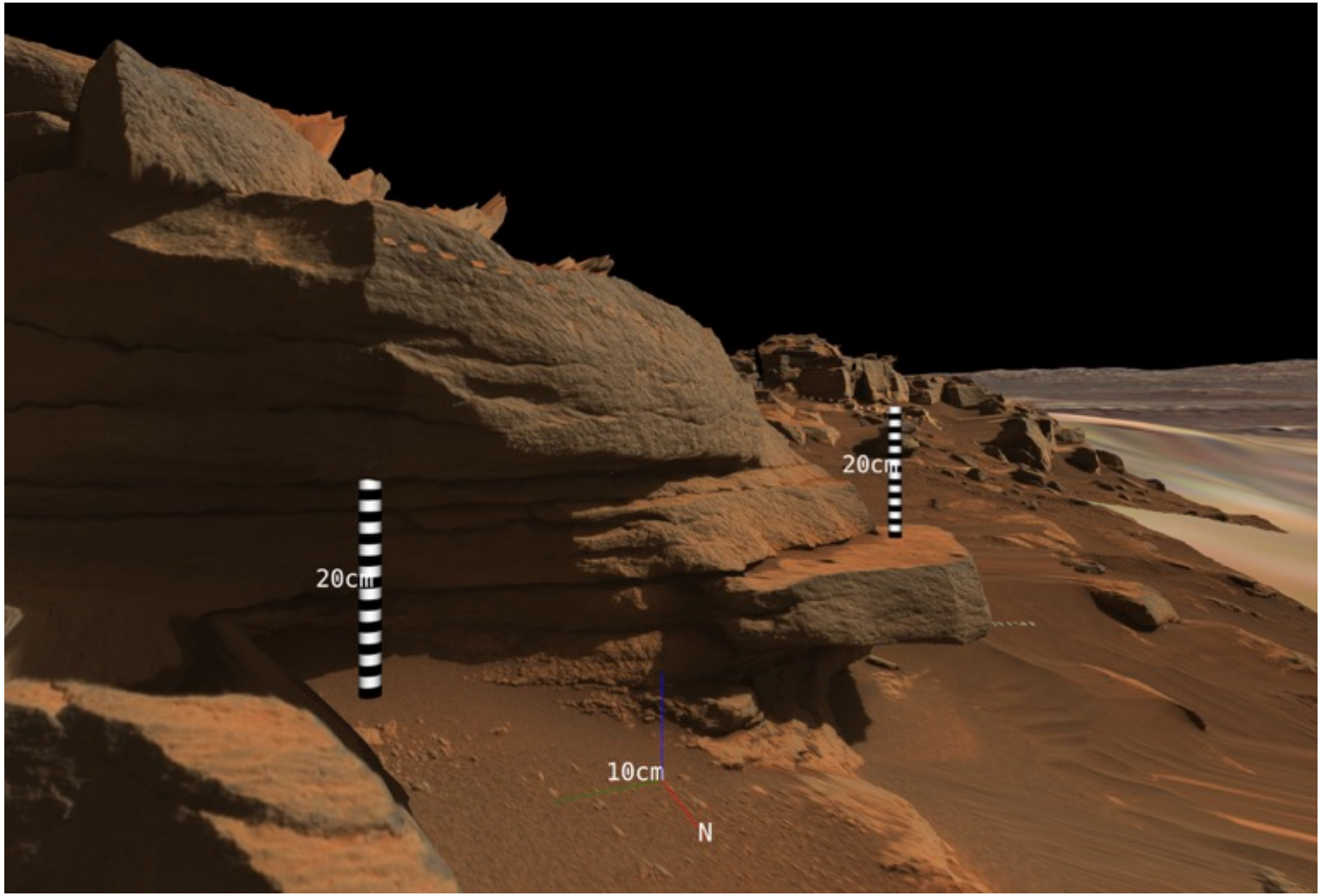

Figure S5. Example 3D reconstruction of an outcrop that was imaged on sol 240 (zcam08264) by Mastcam-Z in the layered rocks of the Bastide member of the Séítah formation. The layers shown here are several centimeters thick and dip with a mean of 4.9°±1.2° and a mean azimuth of 201°±7° (N=6) towards south-southwest. See Materials and Methods. Credits: NASA/JPL/Caltech/MSSS/ASU/JR/VRVis/ÖAW/Andreas Bechtold.

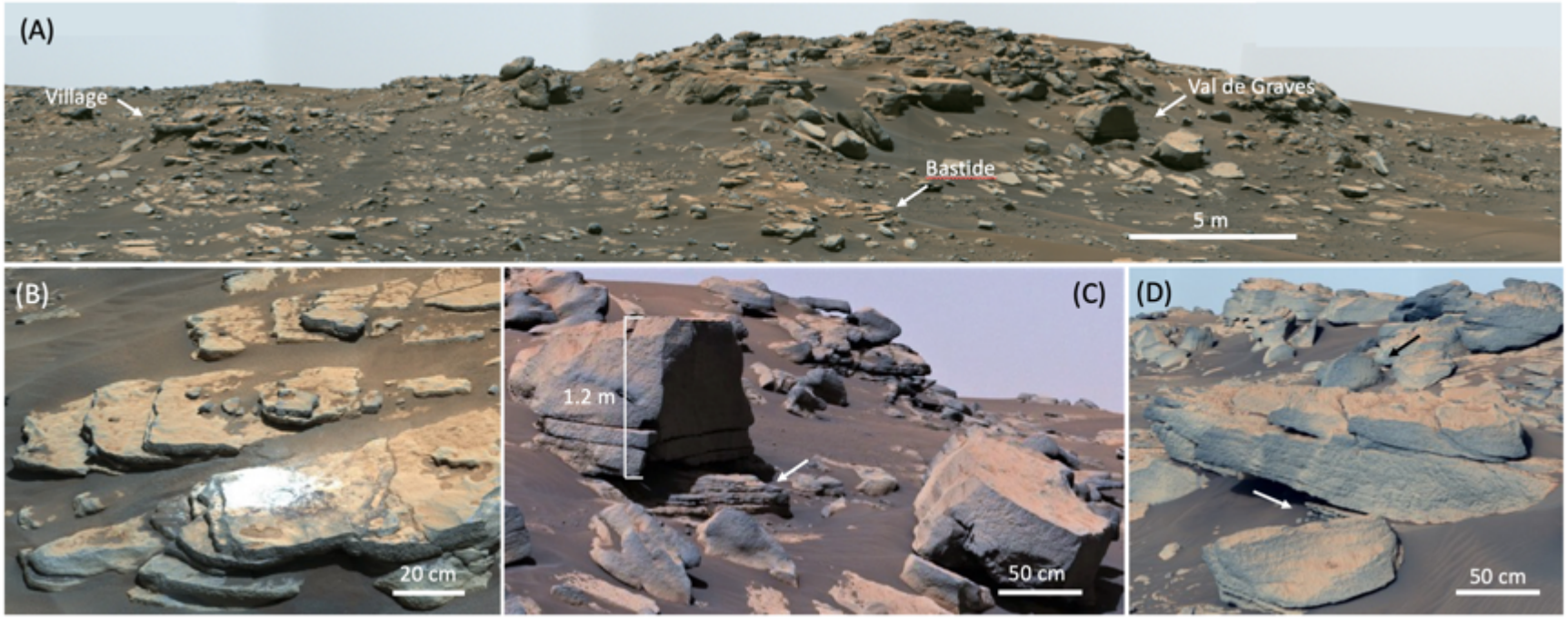

Figure S6. Overlook and characteristic morphologies from Mastcam-Z enhanced color imaging of the Séítah formation in outcrops on Martre ridge in the South Séítah region. (A) Mastcam-Z Sol 202 (zcam08223) mosaic showing thinly layered rocks at the base of the ridge overlain by massive cap rocks with tabular beds. White arrows point to Bastide, Val de Graves, and Village outcrops shown in images (B-D) below. View is towards the NE. (B) Enhanced color mosaic taken on Sol 208 (zcam08240) of the layered Bastide outcrop near the base of Martre ridge and the Garde abrasion patch. View is towards the NW. (C) Mosaic acquired on Sol 208 (zcam08240), showing the transition from thin 1-2 cm-thick layers to massive m-thick beds of the Bastide member visible at the Val de Graves outcrop. The massive boulder on the lower right broke off from the m-thick bed on Val de Graves outcrop. (D) Mosaic of massive and thin layers of Bastide member visible at Village outcrop. Similar to the Val de Graves outcrop, less resistant thin 1-2 cm-thick layers (white arrow) transition to more massive thick beds, resulting in overhangs. The average dip of the layers at this part of Martre ridge is ≈10° to the SW. Overlying the massive beds of the Bastide member are loose pitted boulders (black arrow) that make up the Content member of the Séítah formation. The nature of the fracturing in both (C) and (D) is consistent with the thin layers being less resistant than associated overlying massive beds.

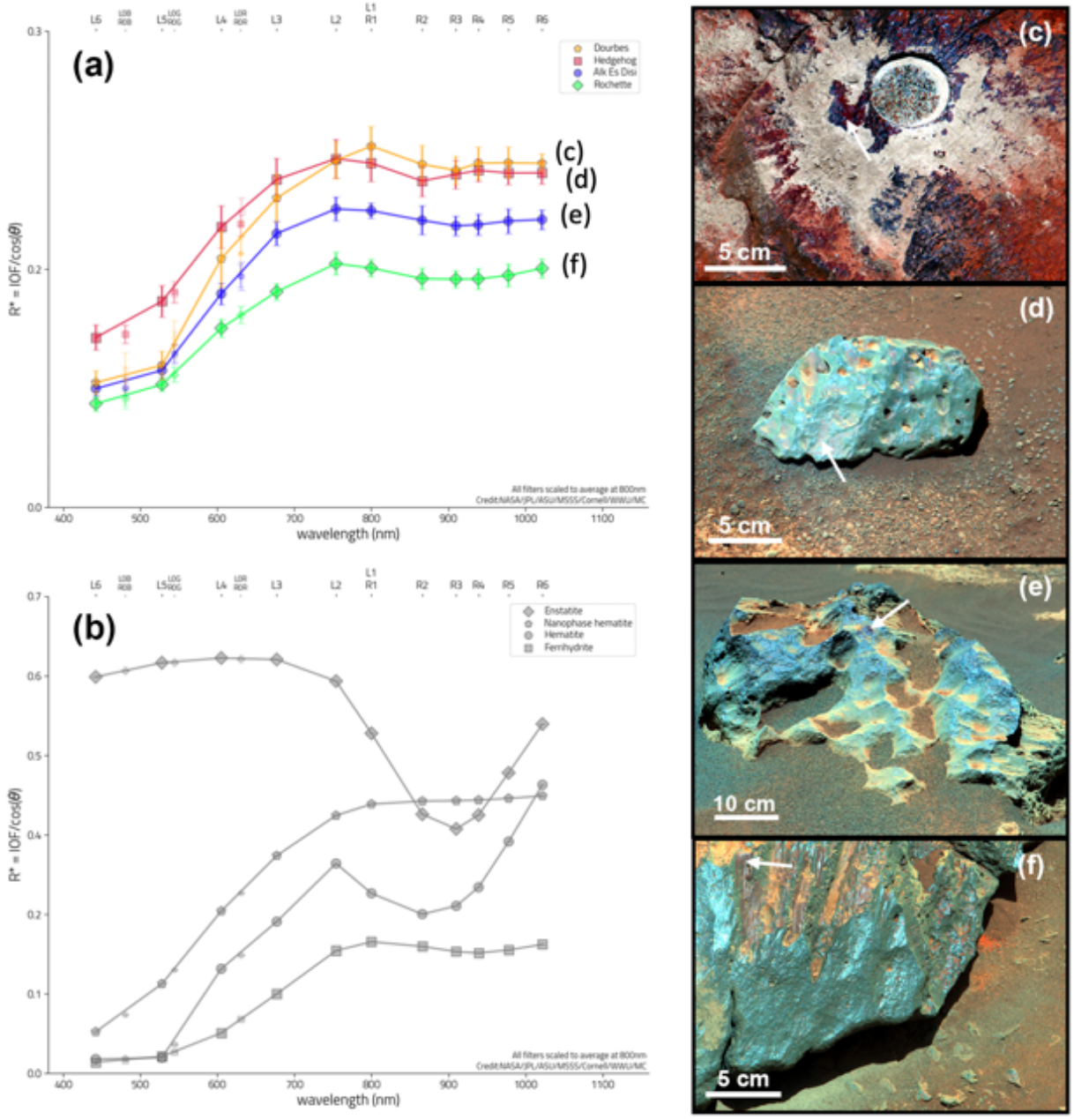

Figure S7. (a) Mastcam-Z spectra of purple-hued coatings, source images shown in c-f. (b) Lab spectra weighted by Mastcam-Z bandpasses. Mastcam-Z enhanced color images of (c) Dourbes (Sol 255, zcam03253); (d) Hedgehog (Sol 37, zcam03108); (e) Alk Es Disi (Sol 91, zcam03141); (f) Rochette (Sol 188, zcam03214). White arrows indicate locations from which spectra were extracted. Error bars represent spatial variance within each region sampled.

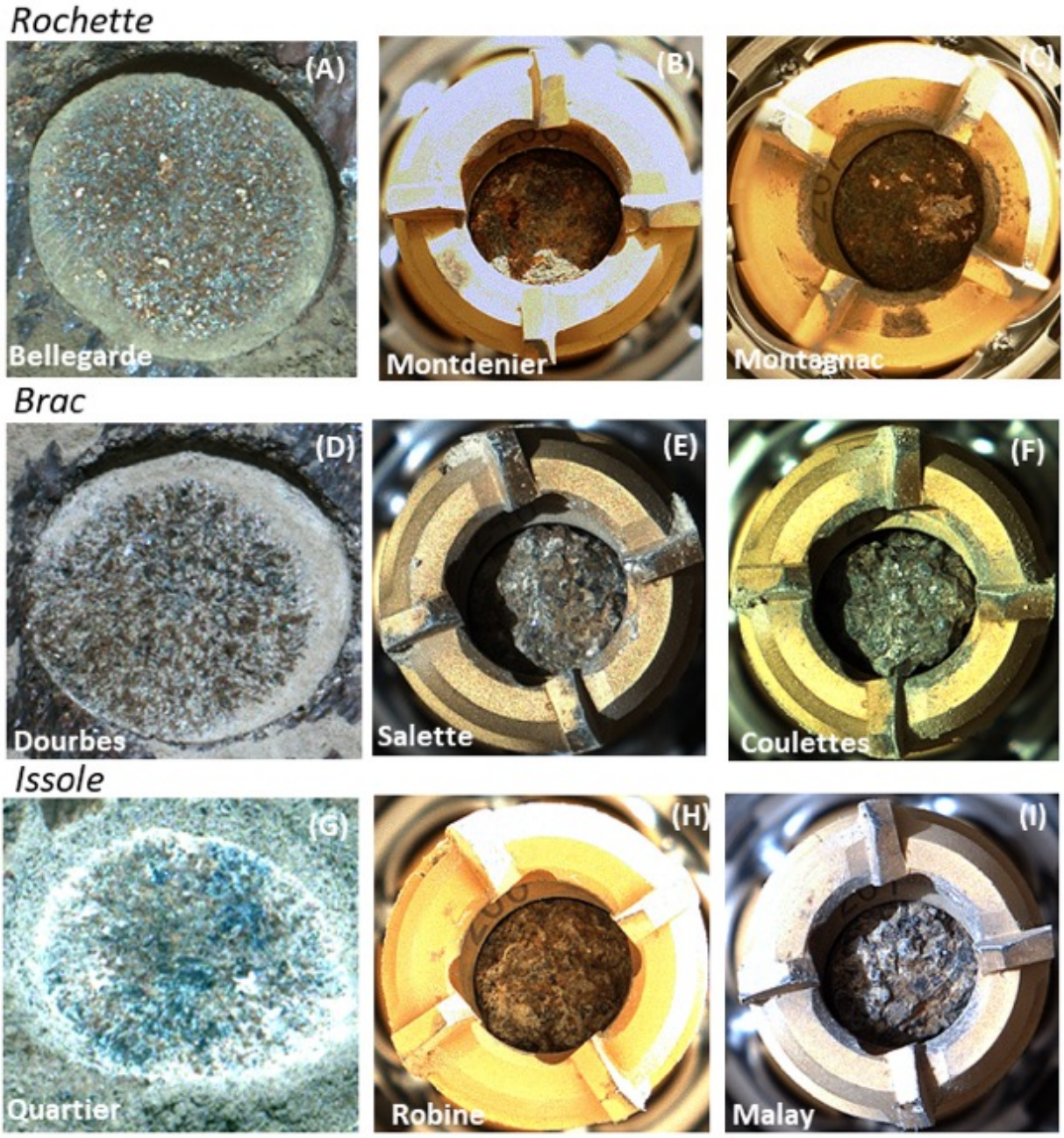

Figure S8. Mastcam-Z images of abrasion patches and core samples for each of the three workspaces sampled as of Sol 337 (Rochette, Brac, Issole). Abrasion patches are shown in the left column and have a 50-mm diameter, followed by the first and second core samples (10-mm diameter) acquired at that workspace (middle and right columns, respectively). (A) Bellegarde abrasion patch Sol 187, zcam03213. (B) Montdenier sample acquired Sol 190, zcam05076. (C) Montagnac sample acquired Sol 196, zcam05076. (D) Dourbes abrasion patch Sol 255, zcam03253. (E) Salette sample acquired Sol 262, zcam05068. (F) Coulettes sample acquired Sol 271, zcam05068. (G) Quartier abrasion patch Sol 295, zcam03273. (H) Robine sample acquired Sol 295, zcam05068. (I) Malay sample acquired Sol 337, zcam05068. See Table 1 for formation and member names associated with these sample sites.

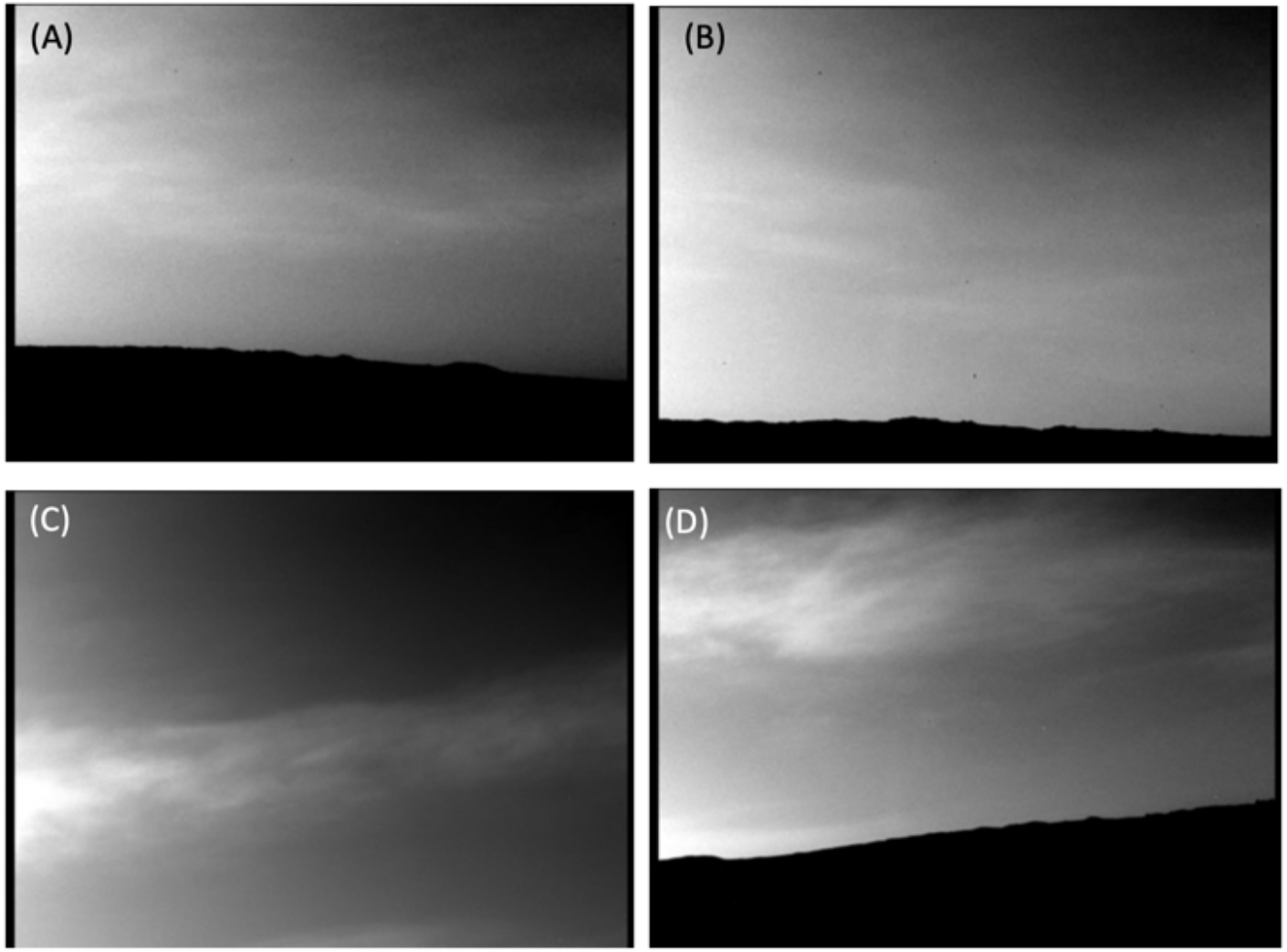

Figure S9: Mastcam-Z examples of ice clouds imaged above Jezero crater. All images acquired at 26-mm focal length (field of view 25.5°×19.1°) using reusable sequence zcam01000. (A) Sol 72; (B) Sol 185; (C) Sol 289; (D) Sol 289.

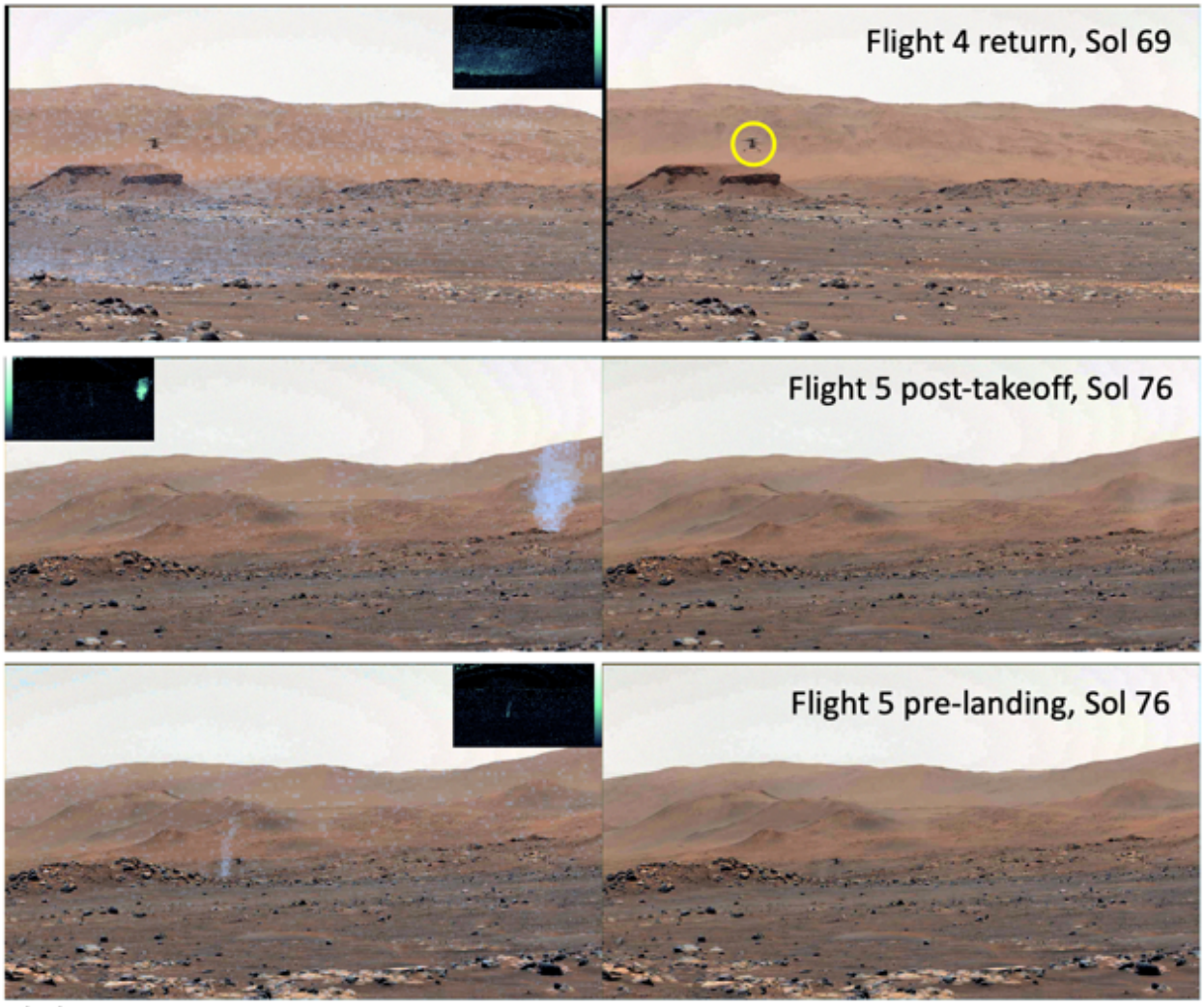

Figure S10: Single Mastcam-Z images extracted from *Ingenuity* flight videos showing lofted dust and background dust devils at 26-mm focal length (field of view 25.5°×19.1°). Each image on the right is an enhanced color stretch (1 to 99%). Each image on the left has a false-color overlay (corresponding to the inset) showing a parameterized dust index, with brighter blue colors corresponding to higher dust devil optical depth. (top row) Flight 4, Sol 69 Mastcam-Z sequence zcam05053. The helicopter is circled in the enhanced color view; (middle row) Flight 5 shortly after takeoff, Sol 76, zcam05060. Two dust devils were observed within a pre-flight part of the video and that later showed up in Navcam images of the flight. The dust devil to the right was in 80 sec of video and had optical depths of about 0.2; the one to the left was in frame for another 40 sec and had optical depths near 0.02. (bottom row) Flight 5, shortly before landing, Sol 76, zcam05060. This dust devil had an optical depth near 0.1 and was observed beyond Adziilii crater, at least 2 km distant and thus > 16 m in diameter. All of these dust devils were moving roughly northwest, which is consistent with prevailing winds from the east-southeast and with the motion of the dust cloud observed in Ingenuity flight 4 on sol 69. Other dust devils showed up in the flight 4 video during take-off, and in images of distant terrain. See links to Supplementary Videos for the full associated Mastcam-Z movies.

Figure S11: Subframed image of the Mastcam-Z radiometric calibration targets (55) acquired by Mastcam-Z through the left-eye broadband (L0) filter at 48-mm focal length on sol 236 in late afternoon (sequence zcam03014). This low-sun frame shows the thick dust rings attracted to the eight strong magnets as well as the relatively clean spots at the center of each patch where the magnetic force repels magnetizable dust. The top surface of the primary target (top) is 10 cm across and the top of the gnomon is 3.75 cm above that surface. The secondary target (bottom) is 8 cm long. The primary target is embellished with a variety of education and public outreach elements (*70*).

List of Supplementary Videos and Interactive 3-D Models

Note: These data provide important visualization support for the results presented in this manuscript. The Ordered Point Clouds (OPCs) used to produce all of the topographic models shown in the supplementary movies were created from PDS-released Mastcam-Z stereo and monoscopic data sets, and are available from sftp://PRoViP-Mastcam-Z-PDS-Released:MQRr63hJdUzVFHYc!@dig-sftp.joanneum.at:2200/ (it is recommended that an sftp client or application is used to connect). In addition, the original 3D model files used in the Sketchfab visualizations linked below are maintained online indefinitely and can be downloaded directly from each of those sites for free.

Videos and www-accessible interactive 3D models that support specific figures, in order:

Movie S1: Figures 2, 3a, 3d, and S1: 3-D video fly-over of regolith and paver rocks at "Peppermint Prickly Pear Pavers" and other locations (with audio).

Figure 3A and S1: 3-D interactive model of Nizhoni. https://skfb.ly/o6BXN

Figure 4E: 3-D interactive model of the sampled rock Rochette, pre-abrasion. https://skfb.ly/o7vUP

Movie S2: Figures 4G and 5: Examples of Mastcam-Z 3-D DTM analyses for stratigraphy and ventifact orientations.

Figure 5B: 3-D interactive model of the Kodiak delta remnant. https://skfb.ly/oorPv

Movie S3: Figures 6A, 6D, 6E, and S6: 3-D video fly-over from an outcrop of the Séítah formation (Figure S6) to Artuby ridge outcrops (Figure 6D and 6E) of the Máaz formation. On the way back the camera stops at an outcrop in the transition zone between the Séítah and Máaz formations (Figure 6A).

Movie S4: Figures 6B and S4: 3-D video fly-over of an outcrop of the Maaz formation at Artuby ridge.

Movie S5: Figure 6C: 3-D video fly-over of the Mure layered outcrop.

Figure 6D: 3-D interactive model of the Mure layered outcrop in the southeast Artuby ridge. https://sketchfab.com/3d-models/m2020-zcam-artuby-sol-173-9fff617e4f6e40378b82e57dd0b58c39

Figures 6 and S4: 3-D interactive model of the Mure layered outcrop farther along on Artuby ridge. https://skfb.ly/opuJX

Figure 8C, 3-D interactive model of the Naat'áanii target in the Dibahi workspace near the Octavia E. Butler landing site. https://skfb.ly/o8VPD

Figure 9G: 3-D interactive model of the Niyol rock target: https://skfb.ly/osEpN

Figure 9F: 3-D interactive model of disturbed soil with wheel tracks at rock named Raton. https://skfb.ly/oow7X

Figure S3B: 3-D interactive model of the abrasion patch at the Guillaumes sampling site. https://skfb.ly/orDII

Movie S6: Figure S3B: 3-D video fly-over of WATSON images of the tailings pile from the "failed" first coring attempt at the Roubion sampling site.

Figure S3C: 3-D interactive model of of WATSON images of the Bellegarde abrasion patch. https://skfb.ly/o8PLU

Figure S3D: 3-D interactive model of of WATSON images of the Garde abrasion patch. https://skfb.ly/o7OwB

Figure S3E: 3-D interactive model of of WATSON images of the Dourbes abrasion patch. https://skfb.ly/o8PLT

Movie S7: Figures S3E, S7C, and S8D: 3-D video fly-over of the of the Brac sampling site.

Figure S4: 3-D interactive model of Artuby ridge. https://skfb.ly/o7Kxs

Movie S8: Figures S5 and S6: 3-D video fly-over of part of Séítah.

Figure S10: Mastcam-Z full videos of *Ingenuity* Flights #4, #5, and others. https://mastcamz.asu.edu/mars-helicopter-flights-caught-on-video/

In addition, the following 3-D fly-over videos provide a general overview/examples of the ways that 3-D images and DTMs support the understanding of scale, sizes, thicknesses, and strikes/dips of features being assessed for stratigraphic and structural analyses, as well as the ways that the authors interrogate the interfaces between rocks and the regolith:

Movie S9: Perseverance Sol 249 visualization from Mastcam-Z 110 mm stereo sequence zcam08272 on the the Séítah formation rock Brac. Scale bar shows 10 cm increments, and several thickness measurements and dip directions are indicated.

Movie S10: Perseverance Sol 204 visualization from Mastcam-Z 110 mm stereo sequence zcam08227 covering light-toned paver rocks of the Naat'áanii member of the Máaz formation. Scale bar shows 10 cm increments.

REFERENCES AND NOTES

1. J. F. Bell III, J. N. Maki, G. L. Mehall, M. A. Ravine, M. A. Caplinger, Z. J. Bailey, S. Brylow, J. A. Schaffner, K. M. Kinch, M. B. Madsen, A. Winhold, A. Hayes, P. Corlies, M. Barrington, R. Deen, E. Cisneros, E. Jensen, K. Paris, K. Crawford, C. Rojas, L. Mehall, J. Joseph, J. B. Proton, N. Cluff, B. Betts, E. Cloutis, A. Coates, A. Colaprete, K. S. Edgett, B. L. Ehlmann, S. Fagents, J. Grotzinger, C. Tate, C. Hardgrove, K. Herkenhoff, B. Horgan, R. Jaumann, J. R. Johnson, M. Lemmon, G. Paar, M. Caballo-Perucha, S. Gupta, C. Traxler, F. Preusker, M. Rice, M. S. Robinson, N. Schmitz, R. Sullivan, M. J. Wolff, The Mars 2020 Perseverance rover Mast Camera Zoom (Mastcam-Z) multispectral, stereoscopic imaging investigation. *Space Sci. Rev.* **217**, 24 (2021).

2. K. M. Stack, N. R. Williams, F. Calef, V. Z. Sun, K. H. Williford, K. A. Farley, S. Eide, D. Flannery, C. Hughes, S. R. Jacob, L. C. Kah, F. Meyen, A. Molina, C. Quantin-Nataf, M. Rice, P. Russell, E. Scheller, C. H. Seeger, W. J. Abbey, J. B. Adler, H. Amundsen, R. B. Anderson, S. M. Angel, G. Arana, J. Atkins, M. Barrington, T. Berger, R. Borden, B. Boring, A. Brown, B. L. Carrier, P. Conrad, H. Dypvik, S. A. Fagents, Z. E. Gallegos, B. Garczynski, K. Golder, F. Gomez, Y. Goreva, S. Gupta, S. E. Hamran, T. Hicks, E. D. Hinterman, B. N. Horgan, J. Hurowitz, J. R. Johnson, J. Lasue, R. E. Kronyak, Y. Liu, J. M. Madariaga, N. Mangold, J. McClean, N. Miklusicak, D. Nunes, C. Rojas, K. Runyon, N. Schmitz, N. Scudder, E. Shaver, J. SooHoo, R. Spaulding, E. Stanish, L. K. Tamppari, M. M. Tice, N. Turenne, P. A. Willis, R. A. Yingst, Photogeologic map of the Perseverance rover field site in Jezero crater constructed by the Mars 2020 Science Team. *Space Sci. Rev.* **216**, 127 (2020).

3. C. I. Fassett, J. W. Head III, Fluvial sedimentary deposits on Mars: Ancient deltas in a crater lake in the Nili Fossae region. *Geophys. Res. Lett.* **32**, L14201 (2003).

4. S. C. Schon, J. W. Head, C. I. Fassett, An overfilled lacustrine system and progradational delta in Jezero crater, Mars: Implications for Noachian climate. *Planet. Space Sci.* **67**, 28–45 (2012).

5. T. A. Goudge, J. F. Mustard, J. W. Head, C. I. Fassett, S. M. Wiseman, Assessing the mineralogy of the watershed and fan deposits of the Jezero crater paleolake system, Mars. *J. Geophys. Res.* **120**, 775–808 (2015).

6. S. Holm-Alwmark, K. M. Kinch, M. D. Hansen, S. Shahrzad, K. Svennevig, W. J. Abbey, Stratigraphic relationships in Jezero crater, Mars: Constraints on the timing of fluvial-lacustrine activity from orbital observations. *J. Geophys. Res. Planets* **126**, e2021JE006840 (2021).

7. S. Shahrzad, K. M. Kinch, T. A. Goudge, C. I. Fassett, D. H. Needham, C. Quantin-Nataf, C. P. Knudsen, Crater statistics on the dark-toned, mafic floor unit in Jezero crater, Mars. *Geophys. Res. Lett.* **46(5)**, 2408–2416 (2019).

8. B. H. Horgan, R. B. Anderson, G. Dromart, E. S. Amador, M. S. Rice, The mineral diversity of Jezero crater: Evidence for possible lacustrine carbonates on Mars. *Icarus* **339**, 113526 (2020).

9. K. A. Farley, K. M. Stack, D. L. Shuster, B. H. N. Horgan, J. A. Hurowitz, J. D. Tarnas, J. I. Simon, V. Z. Sun, E. L. Scheller, K. R. Moore, S. M. McLennan, P. M. Vasconcelos, R. C. Wiens, A. H. Treiman, L. E. Mayhew, O. Beyssac, T. V. Kizovski, N. J. Tosca, J. A. Hurowitz, K. H. Williford, L. S. Crumpler, L. W. Beegle, J. F. Bell III, B. L. Ehlmann, Y. Liu, J. N. Maki, M. E. Schmidt, A. C. Allwood, H. E. F. Amundsen, R. Bhartia, T. Bosak, A. J. Brown, B. C. Clark, A. Cousin, O. Forni, T. S. J. Gabriel, Y. Goreva, S. Gupta, S.-E. Hamran, C. D. K. Herd, K. Hickman-Lewis, J. R. Johnson, L. C. Kah, P. B. Kelemen, K. B. Kinch, L. Mandon, N. Mangold, C. Quantin-Nataf, M. S. Rice, P. S. Russell, S. Sharma, S. Siljeström, A. Steele, R. Sullivan, M. Wadhwa, B. P. Weiss, A. J. Williams, B. V. Wogsland, P. A. Willis, T. A. Acosta-Maeda, P. Beck, K. Benzerara, S. Bernard, A. S. Burton, E. L. Cardarelli, B. Chide, E. Clavé, E. A. Cloutis, B. A. Cohen, A. D. Czaja, V. Debaille, E. Dehouck, A. G. Fairén, D. T. Flannery, S. Z. Fleron, T. Fouchet, J. Frydenvang, B. J. Garczynski, E. F. Gibbons, E. M. Hausrath, A. G. Hayes, J. Henneke, J. L. Jørgensen, E. M. Kelly, J. Lasue, S. Le Mouélic, J. M. Madariaga, S. Maurice, M. Merusi, P.-Y. Meslin, S. M. Milkovich, C. C. Million, R. C. Moeller, J. I. Núñez, A. M. Ollila, G. Paar, D. A. Paige, D. A.

K. Pedersen, P. Pilleri, C. Pilorget, P. C. Pinet, J. W. Rice Jr., C. Royer, V. Sautter, M. Schulte, M. A. Sephton, S. K. Sharma, S. F. Sholes, N. Spanovich, M. St. Clair, C. D. Tate, K. Ucker, S. J. VanBommel, A. G. Yanchilina, M.-P. Zorzano, Aqueously altered igneous rocks on the floor of Jezero crater, Mars. *Science* **377**, eabo2196 (2022).

10. N. Mangold, S. Gupta, O. Gasnault, G. Dromart, J. D. Tarnas, S. F. Sholes, B. Horgan, C. Quantin-Nataf, A. J. Brown, S. Le Mouélic, R. A. Yingst, J. F. Bell III, O. Beyssac, T. Bosak, F. Calef III, B. L. Ehlmann, K. A. Farley, J. P. Grotzinger, K. Hickman-Lewis, S. Holm-Alwmark, L. C. Kah, J. Martinez-Frias, S. M. McLennan, S. Maurice, J. I. Nuñez, A. M. Ollila, P. Pilleri, J. W. Rice Jr., M. Rice, J. I. Simon, D. L. Shuster, K. M. Stack, V. Z. Sun, A. H. Treiman, B. P. Weiss, R. C. Wiens, A. J. Williams, N. R. Williams, K. H. Williford, Evidence for a delta-lake system and ancient flood deposits at Jezero crater, Mars, from the Perseverance rover. *Science* **374**, eabl4051 (2021).

11. R. C. Wiens, A. Udry, O. Beyssac, C. Quantin-Nataf, N. Mangold, A. Cousin, L. Mandon, T. Bosak, O. Forni, S. McLennan, V. Sautter, A. Brown, K. Benzerara, J. R. Johnson, L. Mayhew, S. Maurice, R. B. Anderson, S. M. Clegg, L. Crumpler, T. S. J. Gabriel, P. Gasda, J. Hall, B. Horgan, L. Kah, C. Legett IV, J. M. Madariaga, P. Y. Meslin, A. M. Ollila, F. Poulet, S. K. Sharma, S. Siljeström, J. I. Simon, T. Acosta-Mayeda, C. Alverez-Llamas, S. M. Angel, G. Arana, P. Beck, S. Bernard, T. Bertrand, B. Bousquet, K. Castro, B. Chide, E. Clavé, E. Cloutis, S. Connell, E. Dehouck, G. Dromart, W. Fischer, T. Fouchet, R. Francis, J. Frydenvang, O. Gasnault, E. Gibbons, L. Hausrath, X. Jacob, H. Kalucha, E. Kelly, E. Knutsen, N. Lanza, J. Laserna, J. Lasue, S. Le Mouelic, R. Leveille, G. L. Reyes, R. Lorenz, J. A. Manrique, J. Martinez-Frias, N. Melikechi, T. McConnochie, D. Mimoun, F. Montmessin, J. Moros, N. Murdoch, P. Pilleri, C. Pilorget, P. Pinet, W. Rapin, C. Royer, F. Rull, S. Schroeder, A. Stott, J. Tarnas, N. Turenne, M. Veneranda, D. Vogt, P. Willis, K. M. Stack, K. H. Williford, K. A. Farley; and the SuperCam Team, Compositionally and density stratified igneous terrain in Jezero crater, Mars. *Sci. Adv.* **8**, eabo3399 (2022).

12. E. Ravanis, S. Fagents, C. Newman, B. Horgan, S. Holm-Alwmark, A. J. Brown, J. W. Rice, L. Mandon, M. P. Zorzano, The potential for pyroclastic deposits in the Jezero crater region of

Mars from ash dispersal modeling, in *53rd Lunar and Planetary Science Conference*, LPI Contrib. 2678, abstract #1692 (2022).

13. V. Z. Sun, K. M. Stack, Geologic map of Jezero crater and the Nili Planum region, Mars. U.S. Geological Survey Scientific Investigations Map 3464, pamphlet 14 p., 1 sheet, scale 1:75,000 (2020); https://doi.org/10.3133/sim3464.

14. E. L. Scheller, J. Razzell Hollis, E. L. Cardarelli, A. Steele, L. W. Beegle, R. Bhartia, P. Conrad, K. Uckert, S. Sharma, B. L. Ehlmann, W. J. Abbey, S. A. Asher, K. C. Benison, E. L. Berger, O. Beyssac, B. L. Bleefeld, T. Bosak, A. J. Brown, A. S. Burton, S. V. Bykov, E. Cloutis, A. G. Fairén, L. DeFlores, K.A. Farley, D. M. Fey, T. Fornaro, A. C. Fox, M. Fries, K. Hickman-Lewis, W. F. Hug, J. E. Huggett, S. Imbeah, R. S. Jakubek, L. C. Kah, P. Kelemen, M. R. Kennedy, T. Kizovski, C. Lee, Y. Liu, L. Mandon, F. M. McCubbin, K. R. Moore, B. E. Nixon, J. I. Núñez, C. R. Sanchez-Vahamonde, R. D. Roppel, M. Schulte, M. A. Sephton, S. K. Sharma, S. Siljeström, S. Shkolyar, D. L. Shuster, J. I. Simon, R. J. Smith, K. M. Stack, K. Steadman, B. P. Weiss, A. Werynski, A. J. Williams, R. C. Wiens, K. H. Williford, K. Winchell, B. Wogsland, A. Yanchilina, R. Yingling, M.-P. Zorzano, Aqueous alteration processes and implications for organic geochemistry in Jezero crater, Mars. *Sci. Adv.* **377**, eabo2196 (2022).

15. Y. Liu, M. M. Tice, M. E. Schmidt, A. H. Treiman, T. V. Kizovski, J. A. Hurowitz, A. C. Allwood, J. Henneke, D. A. K. Pedersen, S. J. VanBommel, M. W. M. Jones, A. L. Knight, B. J. Orenstein, B. C. Clark, W. T. Elam, C. M. Heirwegh, T. Barber, L. W. Beegle, K. Benzerara, S. Bernard, O. Beyssac, T. Bosak, A. J. Brown, E. L. Cardarelli, D. C. Catling, J. R. Christian, E. A. Cloutis, B. A. Cohen, S. Davidoff, A. G. Fairén, K. A. Farley, D. O. Flannery, A. Galvin, J. P. Grotzinger, S. Gupta, J. Hall, C. D. K. Herd, K. Hickman-Lewis, R. P. Hodyss, B. H. N. Horgan, J. R. Johnson, J. L. Jørgensen, L. C. Kah, J. N. Maki, L. Mandon, N. Mangold, F. M. McCubbin, S. M. McLennan, K. Moore, M. Nachon, P. Nemere, L. D. Nothdurft, J. I. Núñez, L. O'Neil, C. M. Quantin-Nataf, V. Sautter, D. L Shuster, K. L. Siebach, J. I. Simon, K. P. Sinclair, K. M. Stack, A. Steele, J. D. Tarnas, N. J. Tosca, K. Uckert, A. Udry, L. A. Wade, B. P. Weiss, R. C. Wiens, K. H. Williford, M. Zorzano, A ferroan olivine cumulate on the floor of Jezero crater, Mars. *Science* **377**, 1513–1519.

16. R. A. F. Cas, J. V. Wright, *Volcanic Successions: Modern and Ancient* (Chapman and Hall, 1987), 528 pp.

17. G. R. Osinski, E. Pierazzo, Impact cratering: Processes and products, in *Impact Cratering: Processes and Products*, G.R. Osinski, E. Pierazzo, Eds. (Blackwell Publishing, 2013), pp. 1–20.

18. S.-E. Hamran, D. A. Paige, A. Allwood, H. E. F. Amundsen, T. Berger, S. Brovoll, L. Carter, T. Casademont, L. Damsgård, H. Dypvik, S. Eide, A. G. Fairén, R. Ghent, J. Kohler, M. T. Mellon, D. C. Nunes, D. Plettemeier, P. Russell, M. Siegler, M. J. Øyan, Ground penetrating radar observations of subsurface structures in the floor of Jezero crater, Mars. *Sci. Adv.* **8**, eabp8564 (2022).

19. O. Beyssac, O. Gasnault, B. Chide, E. Clave, A. Cousin, O. Forni, C. Royer, J. R. Johnson, K. Benzerara, S. M. Clegg, P. Meslin, P. Pilleri, P. A. Willis, J. Lasue, L. Mandon, A. Ollila, P. Beck, P. B. Kelemen, E. Dehouck, R. B. Anderson, S. Schröder, A. Udry, T. S. J. Gabriel, T. Bosak, N. Turenne, S. Connell, M. Zorzano, C. Quantin-Nataf, A. J. Brown, J. Manrique, T. Fouchet, V. Sautter, S. Le Mouelic, S. K. Sharma, E.Cloutis, P. C. Pinet, S. Maurice, R. C. Wiens, Mafic chemistry and mineralogy (including olivine) of the coarse-grained regolith analyzed by SuperCam at Jezero crater, Mars, paper presented at the Annual Meeting of the American Geophysical Union, New Orleans, LA, 14 December 2021.

20. R. Sullivan, R. Arvidson, J. F. Bell III, R. Gellert, M. Golombek, R. Greeley, K. Herkenhoff, J. Johnson, S. Thompson, P. Whelley, J. Wray, Wind-driven particle mobility on Mars: Insights from MER observations at “El Dorado” and surroundings at Gusev crater. *J. Geophys. Res.* **113**, E06S07 (2008).

21. C. E. Newman, R. Hueso, M. T. Lemmon, A. Munguira, Á. Vicente-Retortillo, V. Apestigue, G. M. Martínez, D. Toledo-Carrasco, R. Sullivan, K. Herkenhoff, M. de la Torre-Juarez, M. I. Richardson, A. Stott, N. Murdoch, A. Sanchez-Lavega, M. Wolff, I. Arruego-Rodriguez, E. S. Martinez, S. Navarro, J. Gómez-Elvira, L. Tamppari, D. Viúdez-Moreiras, A. Hari, M. Genzer, M. Hieta, R. D. Lorenz, P. Conrad, F. Gómez, T. McConnochie, D. Mimoun, C. Tate, T. Bertrand, J. Bell III, J. Maki, J. A. Rodriguez Manfredi, R. Wiens, B. Chide, S. Maurice,

M. Zorzano, L. Mora, M. Baker, D. Banfield, J. Pla-Garcia, O. Beyssac, A. Brown, B. Clark, A. Lepinette, F. Montmessin, E. Fischer, P. Patel, T. del Río-Gaztelurrutia, T. Fouchet, R. Francis, S. Guzewich, The dynamic atmospheric and aeolian environment of Jezero crater, Mars. *Sci. Adv.* **8**, eabn3783 (2022).

22. G. M. Martínez, C. Newman, A. De Vicente-Retortillo, E. Fischer, N. Renno, M. Richardson, A. G. Fairén, M. Genzer, S. D. Guzewich, R. M. Haberle, A. M. Harri, O. Kemppinen, M. Lemmon, M. D. Smith, M. Torre-Juárez, A. Vasavada, The modern near-surface Martian climate: A review of in-situ meteorological data from Viking to Curiosity. *Space Sci. Rev.* **212**, 295–338 (2017).

23. W. Sheehan, J. F. Bell III, *Discovering Mars: A History of Observation and Exploration of the Red Planet* (University of Arizona Press, 2021), pp. 581–598.

24. M. T. Lemmon, M. J. Wolff, J. F. Bell III, M. D. Smith, B. A. Cantor, P. H. Smith, Dust aerosol, clouds, and the atmospheric optical depth record over 5 Mars years of the Mars Exploration rover mission. *Icarus* **251**, 96–111 (2015).

25. D. S. Colburn, J. B. Pollack, R. M. Haberle, Diurnal variations in optical depth at Mars. *Icarus* **79**, 159–189 (1989).

26. A. R. Vasavada, S. Piqueux, K. W. Lewis, M. T. Lemmon, M. D. Smith, Thermophysical properties along Curiosity's traverse in Gale crater, Mars, derived from the REMS ground temperature sensor. *Icarus* **284**, 372–386 (2017).

27. D. Viúdez-Moreiras, C.E. Newman, M. de la Torre, G. Martínez, S. Guzewich, M. Lemmon, J. Pla-García, M.D. Smith, A.-M. Harri, M. Genzer, A. Vicente-Retortillo, A. Lepinette, J.A. Rodriguez-Manfredi, A.R. Vasavada, J. Gómez-Elvira, Effects of the MY34/2018 global dust storm as measured by MSL REMS in gale crater. *J. Geophys. Res.* **124**, 1899–1912 (2019).

28. D. Viúdez-Moreiras, C.E. Newman, F. Forget, M. Lemmon, D. Banfield, A. Spiga, A. Lepinette, J.A. Rogriguez-Manfredi, J. Gomex-Elvira, J. Pla-Garcia, N. Muller, M. Grott; and

the TWINS/InSight team, Effects of a large dust storm in the near-surface atmosphere as measured by insight in Elysium Planitia, Mars. *J. Geophys. Res.* **125**, e2020JE006493 (2020).

29. R. T. Clancy, M. J. Wolff, P. R. Christensen, Mars aerosol studies with the MGS TES emission phase function observations: Optical depths, particle sizes, and ice cloud types versus latitude and solar longitude. *J. Geophys. Res. Planet* **108**, 2.1–2.20 (2003).

30. M. T. Lemmon, S. D. Guzewich, T. McConnochie, A. de Vicente-Retortillo, G. Martínez, M. D. Smith, J. F. Bell III, D. Wellington, S. Jacob, Large dust aerosol sizes seen during the 2018 Martian global dust event by the *Curiosity* rover. *Geophys. Res. Lett.* **46**, 9448–9456 (2019).

31. M. J. Wolff, J. F. Bell III, P. B. James, R. T. Clancy, S. W. Lee, Hubble space telescope observations of the martian aphelion cloud belt prior to the pathfinder mission: Seasonal and interannual variations. *J. Geophys. Res.* **104**, 9027–9041 (1999).

32. J. N. Maki, D. Gruel, C. McKinney, M. A. Ravine, M. Morales, D. Lee, R. Willson, D. Copley-Woods, M. Valvo, T. Goodsall, J. McGuire, R. G. Sellar, J. A. Schaffner, M. A. Caplinger, J. M. Shamah, A. E. Johnson, H. Ansari, K. Singh, T. Litwin, R. Deen, A. Culver, N. Ruoff, D. Petrizzo, D. Kessler, C. Basset, T. Estlin, F. Alibay, A. Nelessen, S. Algermissen, The Mars 2020 engineering cameras and microphone on the Perseverance rover: A next-generation imaging system for Mars exploration. *Space Sci. Rev.* **216**, 137 (2020).

33. R. Greeley, R. E. Arvidson, P. W. Barlett, D. Blaney, N. A. Cabrol, P. R. Christensen, R. L. Fergason, M. P. Golombek, G. A. Landis, M. T. Lemmon, S. M. McLennan, J. N. Maki, T. Michaels, J. E. Moersch, L. D. V. Neakrase, S. C. R. Rafkin, L. Richter, S. W. Squyres, P. A. De Souza Jr., R. J. Sullivan, S. D. Thompson, P. L. Whelley, Gusev crater: Wind-related features and processes observed by the Mars exploration rover spirit. *J. Geophys. Res.* **111**, E02S09 (2006).

34. R. P. Sharp, Wind-driven sand in Coachella Valley, California. *Geol. Soc. Am. Bull.* **75**, 785–804 (1964).

35. N. T. Bridges, R. Greeley, A. F. C. Haldemann, K. E. Herkenhoff, M. Kraft, T. J. Parker, A. W. Ward, Ventifacts at the Pathfinder landing site. *J. Geophys. Res.* **104**, 8595–8615 (1999).

36. J. E. Laity, N. T. Bridges, Ventifacts on Earth and Mars: Analytical, field, and laboratory studies supporting sand abrasion and windward feature development. *Geomorphology* **105**, 202–217 (2009).

37. J. A. Rodriguez-Manfredi, M. de la Torre Juárez, A. Alonso, V. Apéstigue, I. Arruego, T. Atienza, D. Banfield, J. Boland, M. A. Carrera, L. Castañer, J. Ceballos, H. Chen-Chen, A. Cobos, P. G. Conrad, E. Cordoba, T. Del Río-Gaztelurrutia, A. de Vicente-Retortillo, M. Domínguez-Pumar, S. Espejo, A. G. Fairen, A. Fernández-Palma, R. Ferrándiz, F. Ferri, E. Fischer, A. García-Manchado, M. García-Villadangos, M. Genzer, S. Giménez, J. Gómez-Elvira, F. Gómez, S. D. Guzewich, A.-M. Harri, C. D. Hernández, M. Hieta, R. Hueso, I. Jaakonaho, J. J. Jiménez, V. Jiménez, A. Larman, R. Leiter, A. Lepinette, M. T. Lemmon, G. López, S. N. Madsen, T. Mäkinen, M. Marín, J. Martín-Soler, G. Martínez, A. Molina, L. Mora-Sotomayor, J. F. Moreno-Álvarez, S. Navarro, C. E. Newman, C. Ortega, M. C. Parrondo, V. Peinado, A. Peña, I. Pérez-Grande, S. Pérez-Hoyos, J. Pla-García, J. Polkko, M. Postigo, O. Prieto-Ballesteros, S. C. R. Rafkin, M. Ramos, M. I. Richardson, J. Romeral, C. Romero, K. D. Runyon, A. Saiz-Lopez, A. Sánchez-Lavega, I. Sard, J. T Schofield, E. Sebastian, M. D. Smith, R. J. Sullivan, L. K. Tamppari, A. D. Thompson, D. Toledo, F. Torrero, J. Torres, R. Urquí, T. Velasco, D. Viúdez-Moreiras, S. Zurita; MEDA team, The Mars environmental dynamics analyzer, MEDA. A suite of environmental sensors for the Mars 2020 mission. *Space Sci. Rev.* **217**, 48 (2021).

38. C. E. Newman, M. de la Torre Juárez, J. Pla-García, R. J. Wilson, S. R. Lewis, L. Neary, M. A. Kahre, F. Forget, A. Spiga, M. I. Richardson, F. Daerden, T. Bertrand, D. Viúdez-Moreiras, R. Sullivan, A. Sánchez-Lavega, B. Chide, J. A. Rodriguez-Manfredi, Multi-model meteorological and aeolian predictions for Mars 2020 and the Jezero crater region. *Space Sci. Rev.* **217**, 20 (2021).

39. M. Day, T. Dorn, Wind in Jezero crater, Mars. *Geophys. Res. Lett.* **46**, 3099–3107 (2019).

40. A. G Hayes, J. P. Grotzinger, L. A. Edgar, S. W. Squyres, W. A. Watters, J. Sohl-Dickstein, Reconstruction of eolian bed forms and paleocurrents from cross-bedded strata at Victoria Crater, Meridiani Planum, Mars. *J. Geophys. Res.* **116**, E00F21 (2011).

41. L. K. Fenton, H. C. Carson, T. I. Michaels, Climate forcing of ripple migration and crest alignment in the last 400 kyr in Meridiani Planum, Mars. *J. Geophy. Res.* **123**, 849–863 (2018).

42. J. Baralam, M. Aung, M. P. Golombek, The Ingenuity helicopter on the Perseverance rover. *Space Sci. Rev.* **217**, 56 (2021).

43. S. M. Metzger, J. R. Johnson, J. R. Carr, T. J. Parker, M. Lemmon, Dust devil vortices seen by the Mars Pathfinder camera. *Geophys. Res. Lett.* **26**, 2781–2784 (1999).

44. F. Ferri, P. H. Smith, M. T. Lemmon, N. Renno, Dust devils as observed by Mars Pathfinder. *J. Geophys. Res.* **108**, 5133 (2003).

45. R. Greeley, D. Waller, N. Cabrol, G. Landis, M.T. Lemmon, L. Neakrase, M. P. Hoffer, S. Thompson, P. Whelley, Gusev crater, Mars: Observations of three dust devil seasons. *J. Geophys. Res.* **115**, E00F02 (2010).

46. M. D. Ellehoj, H. P. Gunnlaugsson, K. M. Bean, B.A. Cantor, L. Drube, D. Fisher, B. T. Gheynani, A.-M. Harri, C. Holstein-Rathlou, H. Kahanpää, M. T. Lemmon, M. B. Madsen, M. C. Malin, J. Polkko, P. Smith, L. K. Tamppari, P. A. Taylor, W. Weng, J. Whiteway, Convective vortices and dust devils at the Phoenix Mars Mission landing site. *J. Geophys. Res.* **115**, E00E16 (2010).

47. S. C. Werner, In situ calibration of the Martian cratering chronology. *Meteorit. Planet. Sci.* **54,** 1182–1193 (2019).

48. A. G. Hayes, P. Corlies, C. Tate, J. F. Bell III, J. N. Maki, M. Caplinger, K. M. Kinch, K. Herkenhoff, B. Horgan, J. Johnson, G. Parr, M. S. Rice, E. Jensen, T. M. Kubacki, E. Cloutis, B. Ehlmann, E. Lakdawalla, R. Sullivan, A. Winhold, M. Barrington, A. Parkinson, J. van Beek, P. Caballo-Perucha, E. Cisneros, D. Dixon, C. Donaldson, O. B. Jensen, J. Kuik, K.

Lapo, A. Magee, Pre-flight calibration of the Mars 2020 rover Mastcam Zoom (Mastcam-Z) multispectral, stereoscopic imager. *Space Sci. Rev.* **217**, 29 (2021).

49. K. M. Kinch, M. B. Madsen, J.F. Bell III, J. N. Maki, Z. Bailey, A. G. Hayes, O. B. Jensen, M. Merusi, M. H. Bernth, A. N. Sørensen, M. Hilverda, E. Cloutis, D. Applin, E. Mateo-Marti, J. A. Manrique, G. Lopez-Reyes, A. Bello-Arufe, B. Ehlmann, J. Buz, A. Pommerol, N. Thomas, L. Affolter, K. Herkenhoff, J. R. Johnson, M. Rice, P. Corlies, C. Tate, M. Caplinger, E. Jensen, T. Kubacki, E. Cisneros, K. Paris, A. Winhold, D. Wellington, Radiometric calibration targets for the Mastcam-Z camera on the Mars 2020 rover mission. *Space Sci. Rev.* **216**, 141 (2020).

50. R. J. Reid, P. H. Smith, M. Lemmon, R. Tanner, M. Burkland, E. Wegryn, J. Weinberg, R. Marcialis, D. T. Britt, N. Thomas, R. Kramm, A. Dummel, D. Crowe, B. J. Bos, J. F. Bell III, P. Rueffer, F. Gliem, J. R. Johnson, J. N. Maki, K. E. Herkenhoff, R. B. Singer, Imager for Mars Pathfinder (IMP) image calibration. *J. Geophys. Res.* **104**, 8907–8925 (1999).

51. J. F. Bell, J. N. Maki, Mars 2020 Mast Camera Zoom Data Bundle, from Operations Team, calibrated products. NASA Planetary Data System, doi:10.17189/BS6B-4782 (2021).

52. R. Barnes, S. Gupta, C. Traxler, T. Ortner, A. Bauer, G. Hesina, G. Paar, B. Huber, K. Juhart, L. Fritz, B. Nauschnegg, J. P. Muller, Y. Tao, Geological analysis of Martian rover-derived digital outcrop models using the 3D visualization tool, Planetary Robotics 3D Viewer—Pro3D. *Earth Space Sci.* **5**, 285–307 (2018).

53. P. H. Smith, M. T. Lemmon, Opacity of the Martian atmosphere measured by the Imager for Mars Pathfinder. *J. Geophys. Res.* **104**, 8975–8985 (1999).

54. M. T. Lemmon, M. J. Wolff, M. D. Smith, R. T. Clancy, D. Banfield, G. A. Landis, A. Ghosh, P. H. Smith, N. Spanovich, B. Whitney, P. Whelley, R. Greeley, S. Thompson, J. F. Bell III, S. W. Squyres, Atmospheric imaging results from the Mars Exploration rovers: Spirit and Opportunity. *Science* **306**, 1753–1756 (2004).

55. J. B. Pollack, M. E. Ockert-Bell, M. K. Shepard, Viking Lander image analysis of Martian atmospheric dust. *J. Geophys. Res.* **100**, 5235–5250 (1999)

56. M. G. Tomasko, L. R. Doose, M. T. Lemmon, P. H. Smith, E. Wegryn, Properties of dust in the Martian atmosphere from the Imager on Mars Pathfinder. *J. Geophys. Res.* **104**, 8987–9007 (1999).

57. J. E. Moores, M. T. Lemmon, P. H. Smith, L. Komguem, J. A. Whiteway, Atmospheric dynamics at the Phoenix landing site as seen by the Surface Stereo Imager (SSI). *J. Geophys. Res.* **115**, E00E08 (2010).

58. K. Stamnes, S. C. Tsay, W. J. Wiscombe, K. Jayaweera, Numerically stable algorithm for discrete-ordinate-method radiative transfer in multiple scattering and emitting layered media. *Appl. Optics* **27**, 2502–2509 (1988).

59. I. Laszlo, K. Stamnes, W. J. Wiscombe, S. C. Tsay, The discrete ordinate algorithm, DISORT for radiative transfer, in *Light Scattering Reviews, Volume 11: Light Scattering and Radiative Transfer*, A. Kokhanovsky, Ed. (Springer, 2016), pp. 3–65.

60. K. Connour, M. J. Wolff, N. M. Schneider, J. Deighan, F. Lefevre, S. K. Jain, Another one derives the dust: Ultraviolet dust aerosol properties retrieved from MAVEN/IUVS data. *Icarus* **387**, 10.1016/j.icarus.2022.115177 (2022).

61. M. Newville, T. Stensitzki, D.B. Allen, and A. Ingargiola, LMFIT: Non-Linear Least-Square Minimization and Curve-Fitting for Python. Zenodo 10.5281/zenodo.11813 (2014).

62. M. J. Wolff, M. D. Smith, R. T. Clancy, R. Arvidson, M. Kahre, F. Seelos, S. Murchie, H. Savijärvi, Wavelength dependence of dust aerosol single scattering albedo as observed by the compact reconnaissance imaging spectrometer. *J. Geophys. Res. Planets* **114** E00D04 (2009).

63. M. J. Wolff, R. Todd Clancy, J. D. Goguen, M. C. Malin, B. A. Cantor, Ultraviolet dust aerosol properties as observed by MARCI. *Icarus* **208** 143–155 (2010).

64. M. J. Wolff, R. T. Clancy, M. A. Kahre, R. M. Haberle, F. Forget, B. A. Cantor, M. C. Malin, Mapping water ice clouds on Mars with MRO/MARCI. *Icarus* **332**, 24–49 (2019).

65. M. J. Wolff, M. Lopéz-Valverde, J.-B. Madeleine, R. J. Wilson, M. D. Smith, T. Fouchet, G. T. Delory, Radiative process: Techniques and applications, in *The Atmosphere and Climate of Mars* (Cambridge Univ. Press, 2017), pp. 106–171.

66. S. Maurice, B. Chide, N. Murdoch, R. D. Lorenz, D. Mimoun, R. C. Wiens, A. Stott, X. Jacob, T. Bertrand, F. Montmessin, N. L. Lanza, C. Alvarez-Llamas, S. M. Angel, M. Aung, J. Balaram, O. Beyssac, A. Cousin, G. Delory, O. Forni, T. Fouchet, O. Gasnault, H. Grip, M. Hecht, J. Hoffman, J. Laserna, J. Lasue, J. Maki, J. McClean, P.-Y. Meslin, S. Le Mouélic, A. Munguira, C. E. Newman, J. A. R. Manfredi, J. Moros, A. Ollila, P. Pilleri, S. Schröder, M. de la Torre Juárez, T. Tzanetos, K. M. Stack, K. Farley, K. Williford; SuperCam team, *In situ recording of Mars soundscape*, *Nature* **605**, 653–658 (2022).

67. M. E. Minitti, C. M. Weitz, M. D. Lane, J. L. Bishop, Morphology, chemistry, and spectral properties of Hawaiian rock coatings and implications for Mars. *J. Geophys. Res.* **112**, E05015 (2007).

68. R. F. Kokaly, R. N. Clark, G. A. Swayze, K. E. Livo, T. M. Hoefen, N. C. Pearson, R. A. Wise, W. M. Benzel, H. A. Lowers, R. L. Driscoll, A. J. Klein, “USGS Spectral Library Version 7” (Data Series Rep. 1035, USGS, 2017).

69. E. Cloutis, M. Craig, L. Kaletzke, K. McCormack, L. Stewart, HOSERLab: A new planetary spectrophotometer facility. *Lunar Planet. Sci.* **XXXVII**, 2121 (2006).

70. K. Kinch, M. Hilverda, M. B. Madsen, J. Bell, Calibrating Mars. *Planet. Rep.* **40,** 19–22 (2020).